PAPER

Check for updates

A visible light active, carbon–nitrogen–sulfur co-doped TiO2/g-C3N4 Z-scheme heterojunction as an effective photocatalyst to remove dye pollutants†

Zhen Huang, Shuai Jia, Jie Wei [ID] and Ziqiang Shao [ID]*

Heterojunction formation and heteroatom doping could be viewed as promising strategies for constructing composite photocatalysts with high visible light catalytic activity. In this work, we fabricated a carbon, nitrogen and sulfur co-doped TiO2/g-C3N4 (CNS-TiO2/g-C3N4) Z-scheme heterojunction photocatalyst composite *via* one-step hydrothermal and calcination methods. Compared with pure TiO2 and g-C3N4, the CNS-TiO2/g-C3N4 Z-scheme heterojunction photocatalyst possessed excellent degradation performance under visible light irradiation. Due to the formation of the Z-scheme heterostructure, the utilization rate of the photogenerated electrons–holes generated by the catalyst was increased, which enhanced the catalytic activity. Moreover, the heteroatom doping (C, N and S) could efficiently tailor the band gap of TiO2 and facilitate electron transition, contributing to enhancing the degradation ability under visible light. The CNS-TiO2/g-C3N4-2 exhibited a superior photocatalytic degradation efficiency (k = 0.069 min^{-1}) for methyl orange dye (MO), which is higher than those of pure TiO2 (k = 0.001 min^{-1}) and g-C3N4 (k = 0.012 min^{-1}), showing excellent photocatalytic activity against organic pollutants.

1. Introduction

Globally, the rapid development of industries has caused serious water pollution. Major polluting industries, such as the textile industry, paper industry, and printing and dyeing industry, emit large quantities of wastewater.[1,2] Such industrial wastewater contains organic residues that seriously pollute water resources and even affect human health, which is harmful for a sustainable development.[3–5] Currently, the common methods of sewage treatment include adsorption, flocculation, biofilm and so on,[6] but these traditional processing methods are high in cost and cannot completely degrade pollutants.[7,8]

In 1976, Carey *et al.* discovered that titanium dioxide (TiO2) could successfully dechlorinate polychlorinated biphenyl (PCB) solution after ultraviolet light irradiation,[9] opening a new way of sewage treatment by photocatalysts. Compared with the traditional technology, the photocatalytic oxidation technology possesses outstanding advantages including mild reaction conditions, simple operation, lower energy consumption, and non-secondary pollution, and could be regarded as a promising way to solve environmental problems and achieve pollution control.[2,10,11]

Among a variety of photocatalysts being studied, TiO2 has attracted much attention and been employed as a desirable

Beijing Engineering Research Center of Cellulose and Its Derivatives, School of Materials Science and Engineering, Beijing Institute of Technology, Beijing 100081, P. R. China. E-mail: shaoziqiang@263.net

† Electronic supplementary information (ESI) available. See DOI: 10.1039/d1ra01890f

photocatalytic material owing to its effective photocatalytic activity, stability, non-toxicity and low cost.[12] However, this photocatalytic material still has its disadvantages, which impedes its further application. Its wide band gap (E_g = 3.2 eV)[13] results in a narrow photo response range, which could only be activated by ultraviolet light with λ < 387 nm.[14] Additionally, the quick recombination of the photogenerated electrons and holes (e$^-$/h$^+$) extremely affects the photocatalytic efficiency of TiO2.[12,15] Therefore, it is imperative to develop a TiO2-based photocatalyst with high catalytic activity under sunlight.

To overcome the abovementioned defects, several strategies such as doping metal or non-metal elements and constructing heterojunctions with semiconductors that possess suitable band gaps are applied to improve the photocatalytic performance of TiO2. According to previous reports, graphitized carbon nitride (g-C3N4) with fascinating merits,[15–17] including a similar wide band gap to TiO2, excellent photo-generated electron–hole (e$^-$/h$^+$) transfer ability, simple fabrication and various precursors, could serve as a suitable candidate for constructing a heterojunction with TiO2.[18,19] Currently, constructing a heterojunction between g-C3N4 and TiO2 could be achieved by physical approaches including self-assembly[20] and ball milling,[21] *e.g.* construction of heterostructure g-C3N4/Ag/TiO2 microspheres.[22] However, the heterostructure of TiO2 and g-C3N4 exhibits poor stability when constructed through a simple physical method, which could be attributed to the weak interfacial adhesion.[23] To tackle the above defects, the heterojunction is derived from the combination of physical and chemical approaches and it reveals a desirable performance. A

hydrothermal method was applied to the formation of N-TiO$_2$/O-doped N vacancy g-C$_3$N$_4$ (N-TiO$_2$/CNO$_{NV}$).[24] The optimized photocatalyst N-TiO$_2$/CNO$_{NV}$-2 can achieve about 3 times the tetracycline hydrochloride degradation rate of g-C$_3$N$_4$. A Z-scheme TiO$_2$/g-C$_3$N$_4$/Bi$_2$WO$_6$ heterojunction[25] was also prepared by a hydrothermal method. This kind of heterojunction formed by TiO$_2$ and g-C$_3$N$_4$ exhibits excellent degradation performance in the photocatalytic degradation of organic pollutants such as MO,[26] rhodamine B[27] and tetracyclic tetrasulfonate,[24] displaying an average degradation rate of 90%. However, these TiO$_2$/g-C$_3$N$_4$ heterojunctions contain toxic metals, which may cause secondary pollution during wastewater purification.[26,28] Moreover, the synthesis process is relatively complex and time-consuming and is capable of meeting the requirements of green chemistry.[29,30]

Based on previous studies, in order to reduce the reaction steps and energy consumption, in this work, the synthesis process is modified. Innovatively, carbon, nitrogen and sulfur co-doped TiO$_2$/g-C$_3$N$_4$ (CNS-TiO$_2$/g-C$_3$N$_4$) was prepared through hydrothermal reaction after directly mixing tetrabutyl titanate, melamine and thiourea, and annealing in a nitrogen atmosphere. The dopant heteroatoms, especially the sulfur element, narrow the band gap of CNS-TiO$_2$/g-C$_3$N$_4$, which further widens its light response range from UV to visible light, facilitating the utilization ratio of sunlight on the basis of the heterojunction. Additionally, the Z-scheme heterojunction constructed by g-C$_3$N$_4$ and TiO$_2$ could efficiently separate photo-generated electrons and holes, conducive to generating more $^\bullet$O$_2^-$ and $^\bullet$OH and further improving photocatalytic activity. In short, this work provides new insights into the degradation of organic pollutants with effective photocatalysis.

2. Experimental

2.1 Preparation of g-C$_3$N$_4$

10 g of melamine was placed in a crucible with a lid and annealed at 550 °C for 4 h in an air atmosphere at a heating rate of 2.5 °C min^{-1}, and then fully ground to obtain g-C$_3$N$_4$ after cooling down to room temperature.

2.2 Preparation of CNS-TiO$_2$/g-C$_3$N$_4$ and CN-TiO$_2$/g-C$_3$N$_4$ heterojunction photocatalysts

The evolution of the sample is shown in Scheme 1; the carbon, nitrogen and sulfur co-doped TiO$_2$/g-C$_3$N$_4$ heterojunction (CNS-TiO$_2$/g-C$_3$N$_4$) was synthesized by a hydrothermal method followed by calcination. In this process, 6 mL of tetrabutyl titanate (TBOT) was dropped slowly into a mixed solvent containing

Scheme 1 Schematic illustration of the formation of the CNS-TiO$_2$/g-C$_3$N$_4$ heterojunction.

20 mL of absolute ethanol (EtOH) and 20 mL of DI water, and this solution was stirred for 30 min. Then, 2.2 mmol of melamine and a certain amount of thiourea were added to the above solution with ultrasonication for 30 min. The above solution was transferred to a 50 mL Teflon-lined stainless-steel autoclave and placed in an oven at 150 °C for 10 h. After cooling down to room temperature, the product was washed three times with ethanol and DI water and completely dried in an oven at 60 °C. The as-obtained product was calcined at 300 °C for 4 h at a heating rate of 2.5 °C min^{-1} to prepare CNS-TiO$_2$/g-C$_3$N$_4$ heterojunctions. According to the amount of thiourea (1.1, 2.2, 4.4 mmol), the obtained CNS-TiO$_2$/g-C$_3$N$_4$ heterojunctions were denoted as CNS-TiO$_2$/g-C$_3$N$_4$-X (X = 1, 2, 3).

CN-TiO$_2$/g-C$_3$N$_4$ was synthesized by the same method, except that thiourea was not added before the hydrothermal reaction.

2.3 Characterization

Field emission scanning electron microscopy (SEM, Hitachi S-4800 system, Japan) and field emission transmission electron microscopy (TEM, JEM-2100, Japan) were applied to obtain the morphological images of the samples. In order to determine the crystal structure and phase compositions of the samples, X-ray diffraction (XRD) patterns were collected over the 2θ range of 10–80° on a Bruker D8 system (Germany) equipped with a Cu K$_\alpha$ radiation source. Fourier transform infrared (FT-IR) spectra were measured to identify the types of functional groups with a Nicolet IS10 (Nicolet Co.) FT-IR spectrophotometer using the KBr pellet technique. X-ray photoelectron spectroscopy (XPS) patterns were recorded on an ESCALAB 250Xi (Thermo Co.) with a photoelectron take-off angle of 45°. UV-visible diffuse-reflectance spectra (UV-vis DRS) were obtained by using a UV-visible spectrophotometer (Du800, Beckman Co.) with BaSO$_4$ as a reflectance standard. Photoluminescence (PL) spectra were collected using a fluorescence spectrophotometer (OmniPL, Beijing Zhuoli, China) at an excitation wavelength of 320 nm.

The electrochemical test was performed on an electrochemical workstation (CHI760E). Transient photocurrent (TPC) measurements and electrochemical impedance spectroscopy (EIS) were performed in a 0.1 M Na$_2$SO$_4$ aqueous electrolyte with a standard three-electrode configuration. Fluorine doped tin oxide (FTO) electrodes coated with a catalyst, a platinum wire, and a saturated calomel electrode (SCE) were used under visible-light (λ > 420 nm) as the working electrode, pair electrode, and reference electrode, respectively.

2.4 Evaluation of photocatalytic activity

The ability of the photocatalyst prepared above to degrade methyl orange (MO) dye was studied. A 300 W xenon lamp with a 420 nm cut-off filter (CEL-HXUV300-(T3), Beijing Zhongjiao Jinyuan Technology Co., Ltd.) was employed as a visible light source. Generally, 20 mg of photocatalyst was dispersed in a quartz reactor containing 50 mL of MO solution (20 mg L^{-1}). After the suspension was stirred in the dark for 45 min to reach the adsorption–desorption equilibrium, the reactor was irradiated vertically with visible light. During this process, 2 mL of the reaction solution was withdrawn at a given interval (10 min) and
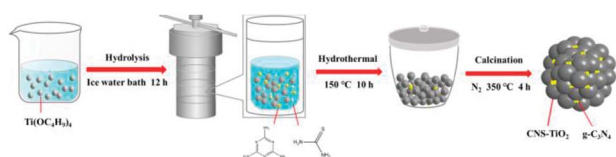
was filtered through a 0.45 μm filter. Finally, the MO degradation efficiency was calculated from the absorbance of the collected filtrate measured by UV-vis spectrophotometry at 465 nm.

The CNS-TiO_2/g-C_3N_4-X after photocatalytic degradation was collected by centrifugal separation, washed with deionized water, and then subjected to 5 cycles of degradation experiments to prove its reusability and stability. In each repeat experiment, the ratio of the catalyst to dye remained constant.

3. Results and discussion

3.1 Morphology, structure and surface chemical state

The morphologies and the microstructures of the samples were characterized by SEM and TEM. It can be seen from Fig. 1a that the TiO_2 particles with a diameter of around 20 nm are densely accumulated together. The morphology of the obtained graphitized carbon nitride is shown in Fig. 1b, which presents a stacked sheet structure. However, there is no regular shape, and the particle size is inhomogeneous in Fig. 1c. As shown in Fig. 1d, the CNS-TiO_2/g-C_3N_4-2 presents a relatively regular spherical shape with a diameter of about 400–600 nm. A detailed microscopic morphology can be observed from TEM and HRTEM.

A more clear observation of the morphologies is shown in the TEM images of CNS-TiO_2/g-C_3N_4-2 (Fig. 2a), which indicates that the microsphere is composed of numerous TiO_2 particles, which are closely gathered together. Fig. 2b shows that the particle size of TiO_2 in CNS-TiO_2/g-C_3N_4-2 is about 5–10 nm. As marked in high-resolution TEM (HRTEM) images (Fig. 2c), it can be clearly seen that the lattice spacing of 0.35 nm corresponds to the (101) crystalline plane of anatase TiO_2,[31] which also proves that the TiO_2 of CNS-TiO_2/g-C_3N_4-2 is anatase type.[32] At the same time, we can see that the TiO_2 is embedded in g-C_3N_4.

Furthermore, the SEM-EDS mapping images shown in Fig. 2d demonstrate a uniform distribution of C, N, O, S and Ti elements in the CNS-TiO_2/g-C_3N_4-2, evidencing that the S element is incorporated into the CNS-TiO_2/g-C_3N_4-2 composite catalyst.
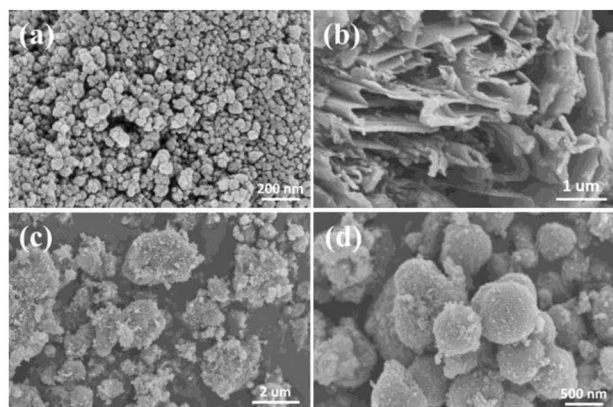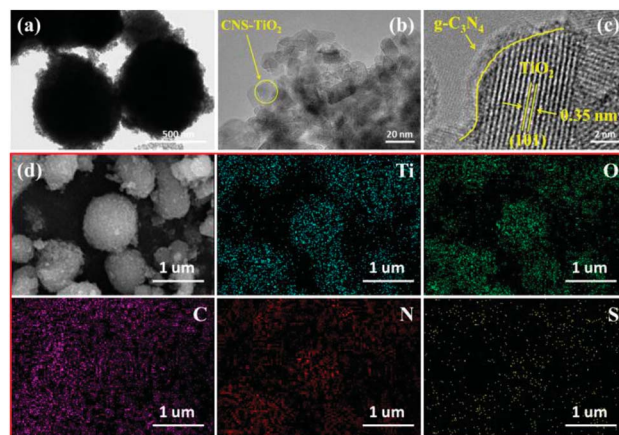

Fig. 2 TEM images of (a and b) CNS-TiO_2/g-C_3N_4-2; HRTEM images of (c) CNS-TiO_2/g-C_3N_4-2; (d) SEM-EDS mapping images of CNS-TiO_2/g-C_3N_4-2.

The crystal structure of each component of the prepared catalyst was characterized by XRD analysis to confirm the formation of the heterojunction. As exhibited in Fig. 3a, the diffraction peaks at 13.0° and 27.8° are assigned to the (100) and (002) facets of g-C_3N_4, respectively, which are related to the continuous 3-s-triazine network and accumulation of a conjugated aromatic system, implying the successful synthesis of g-C_3N_4.[33] For the TiO_2-based heterojunction samples, the diffraction peaks at 25.4°, 38.0°, 48.0°, 53.9°, 55.2°, 62.7°, 68.8°, 70.2° and 75.3° correspond to the (101), (004), (200), (105), (211), (204), (116) and (220) crystal planes, coinciding with the standard phase peak of anatase titanium dioxide (JCPDS: # 21-2172).[34] In the XRD patterns of CNS-TiO_2/g-C_3N_4-X and CN-TiO_2/g-C_3N_4, the diffraction peak of g-C_3N_4 is also displayed, and its intensity is relatively weak due to the lower content of g-C_3N_4.

FTIR measurements were performed to analyze the functional groups in the as-synthesized composite material, and the results are shown in Fig. 3b. For pure TiO_2, the broad absorption peak at 400–800 cm^{-1} corresponds to the stretching vibrational modes of Ti–O–Ti, and the absorption peaks at 1624 and 3412 cm^{-1} are derived from the bending and stretching vibration of O–H, respectively, which is attributed to H_2O molecules or hydroxyl groups adsorbed on the TiO_2 surface.[35] For pure g-C_3N_4, the N–H stretching vibration, C–N and C=N
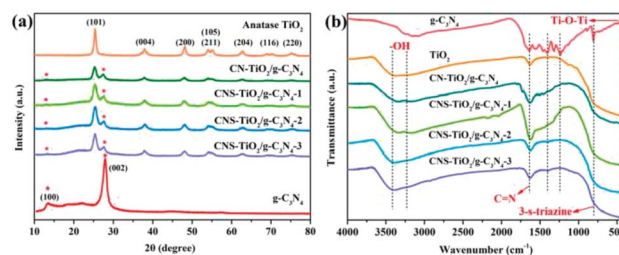

Fig. 1 SEM images of (a) TiO_2, (b) g-C_3N_4, (c) CN-TiO_2/g-C_3N_4, and (d) CNS-TiO_2/g-C_3N_4-2.

Fig. 3 (a) XRD patterns of TiO_2, g-C_3N_4, CNS-TiO_2/g-C_3N_4-X and CN-TiO_2/g-C_3N_4 heterojunction catalysts. (b) FTIR spectra of TiO_2, g-C_3N_4, CNS-TiO_2/g-C_3N_4-X and CN-TiO_2/g-C_3N_4 heterojunction catalysts.

stretching vibration and 3-*s*-triazine ring bending vibration are observed at 3170–3450, 1210–1680 and 815 cm^{-1}, respectively.[36] Although the characteristic absorption peaks of TiO_2 and g-C_3N_4 coexist in the as-prepared CNS-TiO_2/g-C_3N_4-*X* and CN-TiO_2/g-C_3N_4 samples, the typical 3-*s*-triazine ring peak at 815 cm^{-1} is almost absent on account of the small amount of g-C_3N_4 in the composite catalyst and the masking effect of the Ti–O–Ti, consistent with XRD results.

XPS analysis was carried out to identify the chemical states and element composition in the CNS-TiO_2/g-C_3N_4-2 composite catalyst, and the results are displayed in Fig. 4. The peaks at 458.5 and 464.2 eV in the high-resolution Ti 2p XPS spectrum (Fig. 4a) correspond to the split peaks of Ti $2p_{1/2}$ and Ti $2p_{3/2}$, respectively. It is worth mentioning that both peaks of Ti ($2p_{1/2}$ and $2p_{3/2}$) in the CNS-TiO_2/g-C_3N_4-2 sample shift negatively compared with those of pure TiO_2. This is because some Ti–O is replaced by Ti–C, Ti–N and Ti–S, and the electronegativity of carbon, nitrogen and sulfur atoms is weaker than that of oxygen atoms, resulting in a stronger electron cloud density of Ti. Another reason is that g-C_3N_4 has a higher Fermi level (*vs.* vacuum level) than TiO_2. Therefore, when g-C_3N_4 and TiO_2 are in contact, the electrons will spontaneously migrate from g-C_3N_4 to TiO_2 until their Fermi levels reach equilibrium.[37,38] The O 1s XPS spectra exhibit three fitted peaks at 529.8, 531.2, and 531.8 eV in Fig. 4b, corresponding to the Ti–O (lattice oxygen of anatase TiO_2), Ti–O–N (or Ti–O–S) and C–O (or C–S) bonds, respectively.[38] Due to the migration of electrons, the binding energy of lattice O of CNS-TiO_2/g-C_3N_4-2 displays a slightly negative shift in comparison with that of pure TiO_2. The high-resolution C 1s XPS spectra of CNS-TiO_2/g-C_3N_4-2 (Fig. 4c) could be fitted by alkyl or adventitious carbon (285.1 eV), C–C (286.3 eV) and N=C–(N)$_2$ (288.6 eV).[39,40] The N 1s XPS curves (Fig. 4d) are composed of three peaks at 399.2, 400.1 and 400.6 eV, which are attributed to sp^2-hybridized N (C–N=C), Ti–O–N and tertiary nitrogen N–(C)$_3$, respectively. When comparing the C 1s and N 1s XPS spectra of g-C_3N_4, the CNS-TiO_2/g-C_3N_4-2 possesses higher binding energies than g-C_3N_4 in

the absence of light illumination, which is due to the transfer of electrons from g-C_3N_4 to TiO_2 to achieve Fermi level equilibrium. The above results prove that a C, N, and S co-doped TiO_2/g-C_3N_4 heterojunction was successfully prepared *via* one-step hydrothermal reaction and anaerobic calcination.

3.2 Optical absorption properties

Ultraviolet-visible-near-infrared diffuse-reflectance spectroscopy (UV-vis DRS) was performed to analyze the absorption properties and band gap of the g-C_3N_4, TiO_2, CN-TiO_2/g-C_3N_4 and CNS-TiO_2/g-C_3N_4-*X* samples. As shown in Fig. 5a, pure TiO_2 could be excited in the ultraviolet region, and its absorption edge is about 382 nm. The light absorption of pure g-C_3N_4 extends from the ultraviolet region to the visible region of 464 nm. Obviously, the CN-TiO_2/g-C_3N_4 sample displays a new absorption peak at 390–550 nm, showing a red-shift compared with pure TiO_2. It is also worth noting that the absorption peak of CNS-TiO_2/g-C_3N_4 widens, and the absorption edge extends to around 550 nm, suggesting that the electrons could achieve transition in contrast to that in the case of pure TiO_2 and g-C_3N_4 under the same UV irradiation.[41] These results could be attributed to the C, N and S elements doped into TiO_2, contributing to the expansion of the photo-response range in CNS-TiO_2/g-C_3N_4-*X* samples and further enhancing the catalytic performance. More importantly, it is the CNS-TiO_2/g-C_3N_4-*X* that possesses a wider absorption edge and higher absorption intensity than CN-TiO_2/g-C_3N_4, indicating that the S doping could induce a visible light response and play a vital role in tuning the band gap structure in the as-prepared products.

Additionally, the band gap energies of TiO_2, g-C_3N_4, CN-TiO_2/g-C_3N_4 and CNS-TiO_2/g-C_3N_4-*X* samples are determined according to the Tauc diagram converted from the Kubelka–Munk function:[25] $\alpha = \dfrac{(1-R)^2}{2R}$, where α represents the Kubelka–Munk function and R is the reflectivity. The curve graph of $\alpha \sim \lambda$ can be transformed into the curve graph corresponding to $(\alpha h\nu)2 \sim h\nu$, where $h\nu$ is the energy,[22] and $h\nu = \dfrac{1240}{\lambda}$ intercepting the tangent to the *X* axis can be a good approximation of the E_g of the samples. The related results are depicted in Fig. 5b, and the band gaps of pure TiO_2 and g-C_3N_4 are 3.08 and 2.41 eV, respectively.[42] The band gap of the CN-TiO_2/g-C_3N_4, as expected, is narrower than that of pure TiO_2
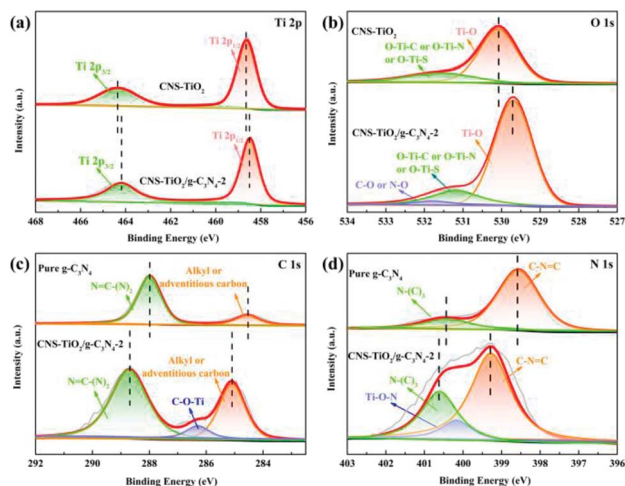

Fig. 4 High-resolution XPS spectra of Ti 2p (a), O 1s (b), C 1s (c), and N 1s (d) in CNS-TiO_2/g-C_3N_4-2.
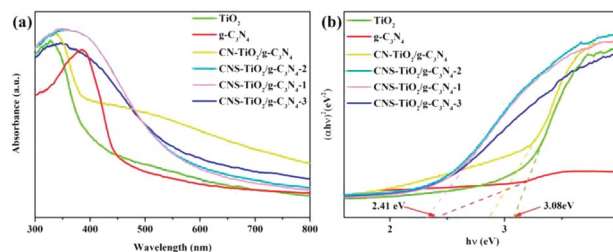

Fig. 5 (a) UV-vis diffuse reflectance spectra and (b) plots of transformed Kubelka–Munk function *versus* the energy of light for the samples.

after compounding with g-C$_3$N$_4$, implying the positive effect of the heterojunction and heteroatom doing. For the CNS-TiO$_2$/g-C$_3$N$_4$-X samples, the band gap values are 2.38 (CNS-TiO$_2$/g-C$_3$N$_4$-1), 2.35 (CNS-TiO$_2$/g-C$_3$N$_4$-2) and 2.24 eV (CNS-TiO$_2$/g-C$_3$N$_4$-3), respectively, revealing an approximated band gap to that of the pure g-C$_3$N$_4$, which indicates that the doped S element is capable of reducing the band gap effectively.[43] Therefore, the heterojunction derived from the g-C$_3$N$_4$ and TiO$_2$ matrix combined with the heteroatom doping (C, N and S) in the TiO$_2$ matrix could not only accommodate the band gap to facilitate electron transition, but also expand the absorption width to ensure high utilization ratio of visible light.

3.3 Photocatalytic activity

MO, a common dye, used in printing and dyeing textiles could cause organic pollution in the textile field. In this study, MO was used as a target pollutant to evaluate the photocatalytic activity of the as-prepared samples under visible light ($\lambda > 420$ nm), and the final results are shown in Fig. 6. After stirring for 45 min, each sample reaches the adsorption–desorption equilibrium in MO solution without light (Fig. 6a). The pure TiO$_2$ has almost no photodegradation effect on MO under visible light, implying a poor photocatalytic effect. However, the photodegradation efficiency values of g-C$_3$N$_4$ and CN-TiO$_2$/g-C$_3$N$_4$ could reach 86.4% and 92.8%, respectively, after light exposure for 80 min, which suggests that the incorporation of g-C$_3$N$_4$ could effectively ameliorate the defects originating from pure TiO$_2$. With doping S atoms into CN-TiO$_2$/g-C$_3$N$_4$, the photodegradation efficiency of the CNS-TiO$_2$/g-C$_3$N$_4$-X (X = 1, 2, 3) for MO reached more than 95% under the same conditions, and the CNS-TiO$_2$/g-C$_3$N$_4$-2 exhibits an excellent photodegradation efficiency of 99.8%, demonstrating that the MO is almost completely degraded under the same conditions.

According to the equation $\ln\left(\dfrac{C}{C_0}\right) = kt$,[44] the MO degradation rate constant of each sample was calculated, and the corresponding reaction kinetics data of each catalyst sample are plotted in Fig. 6b, and are fitted to a pseudo first-order kinetics reaction. The equilibrium constant (k) of the TiO$_2$, g-C$_3$N$_4$, CN-TiO$_2$/g-C$_3$N$_4$ and CNS-TiO$_2$/g-C$_3$N$_4$-X (X = 1, 2, 3) samples in our work are 0.001, 0.012, 0.035, 0.042, 0.043, and 0.069 min^{-1} as shown in Fig. 6c. The k of pure TiO$_2$ is almost zero due to the wide band gap of TiO$_2$, and hence the pure TiO$_2$ could only be excited by short-wavelength UV light to generate electrons and holes.[45] However, the sample CNS-TiO$_2$/g-C$_3$N$_4$-2 with the best catalytic activity has a degradation rate of 0.069 min^{-1}, which is

5.83 and 1.98 times those of g-C$_3$N$_4$ and CN-TiO$_2$/g-C$_3$N$_4$, respectively, benefiting from the fabrication of a heterojunction and the heteroatom doping in TiO$_2$. Meanwhile, CNS-TiO$_2$/g-C$_3$N$_4$-2 is a heterojunction formed by g-C$_3$N$_4$, with a relatively narrow band gap, and TiO$_2$. Due to the different band gap widths of g-C$_3$N$_4$ and TiO$_2$, the positions of the valence band (VB) and conduction band (CB) are also different. The energy level differences between the two semiconductors can increase the separation rate of photogenerated electron–hole pairs, thereby further shifting the spectral response range of the composite catalyst to the visible light region, and the photocatalytic activity is optimized compared with the single composition. Simultaneously, the dopant atoms (C, N and S) could replace some O^{2-} and Ti^{4+} atoms in TiO$_2$, forming a doped energy level close to the valence band,[46,47] which could efficiently narrow the forbidden band width of TiO$_2$ on the basis of the heterojunction and further improve the visible light catalytic activity.

The reusability of catalyst materials is significant to assess its stability for continuous use. The CNS-TiO$_2$/g-C$_3$N$_4$-2 was repeatedly applied to MO dye degradation to evaluate its reusability (Fig. S1†). The experimental results indicate that the CNS-TiO$_2$/g-C$_3$N$_4$-2 composite catalyst possesses excellent chemical stability and light corrosion resistance and can be used as a new material for degrading organic pollutants in wastewater.

Since MO dye may be degraded via the photosensitization pathway, we performed the supplemental phenol degradation experiment. Phenol, a colorless monocyclic aromatic organic compound, was used as a probe to characterize the photocatalytic performance of CNS-TiO$_2$/g-C$_3$N$_4$. As shown in Fig. 7a, the pure TiO$_2$ had almost no photodegradation effect on phenol under visible light. Among all samples, the CNS-TiO$_2$/g-C$_3$N$_4$-2 had the highest removal efficiency for phenol and 97.6% phenol was decomposed in 60 min. The photocatalytic activity of CNS-TiO$_2$/g-C$_3$N$_4$ heterojunction photocatalysts for phenol degradation was higher than that of single components. The kinetics of photocatalytic phenol degradation over all catalysts was fitted, and all samples as shown in Fig. 7b conformed to the first-order kinetics model. The photocatalytic phenol degradation rate of CNS-TiO$_2$/g-C$_3$N$_4$-2 was calculated to be 0.04503 min^{-1}, which was 1.41 and 3.67 times higher than that of CN-TiO$_2$/g-C$_3$N$_4$ and g-C$_3$N$_4$, respectively. The above results indicated that CNS-TiO$_2$/g-C$_3$N$_4$ not only has excellent photocatalytic degradation activity for organic dye MO, but also for phenol.

3.4 Possible photocatalytic mechanism

The transport efficiency of photogenerated charges plays a decisive role in photocatalytic activity. In order to investigate
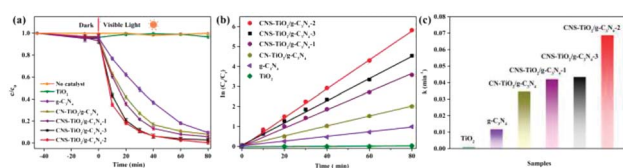

Fig. 6 (a) Visible light catalytic degradation of MO, (b) pseudo-first-order kinetics curves of different catalysts, and (c) pseudo-first-order rate constant k with different catalysts.
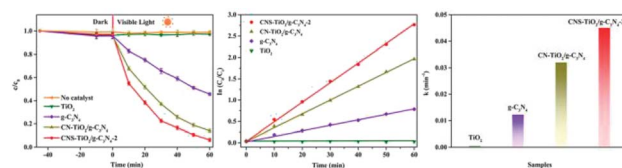

Fig. 7 (a) Visible light catalytic degradation of phenol, (b) pseudo-first-order kinetics curves of different catalysts, and (c) pseudo-first-order rate constant k with different catalysts.
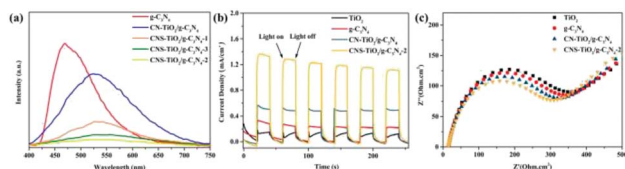
Fig. 8 (a) PL emission spectra, (b) transient photocurrent (TPC) responses and (c) electrochemical impedance (EIS) spectra.

the photocatalytic mechanism of CNS-TiO$_2$/g-C$_3$N$_4$-X, PL, TPC, and EIS analyses were carried out. PL analysis is usually used to detect the recombination efficiency of electrons and holes in a sample. The higher the recombination efficiency of electrons and holes, the stronger the PL intensity.[48] The PL properties of each sample are shown in Fig. 8a. It can be found that the PL intensity of g-C$_3$N$_4$ is stronger at 460 nm, while the peak of the PL intensity of CN-TiO$_2$/g-C$_3$N$_4$ and CNS-TiO$_2$/g-C$_3$N$_4$-X (X = 1, 2, 3) appears at 530 nm, and the intensity is largely reduced. This demonstrates that the combination of TiO$_2$ and g-C$_3$N$_4$ facilitates the separation of photogenerated electrons and holes. Moreover, the difference in the doping amount of the S element also affects the PL intensity. The CNS-TiO$_2$/g-C$_3$N$_4$-2 with the best photocatalytic degradation performance shows the lowest PL intensity, which is consistent with the facts.

To further investigate the productivity of photogenerated charge carriers, the TPC responses curves under visible light are presented in Fig. 8b. Obviously, the CNS-TiO$_2$/g-C$_3$N$_4$-2 heterojunction has the higher photocurrent density than single phase TiO$_2$ and g-C$_3$N$_4$. The photocurrent density is closely related to the lifetime of charge carriers under illumination.[49] The hole–electron pairs have higher separation efficiency indicating an enhanced lifetime of charge carriers in the CNS-TiO$_2$/g-C$_3$N$_4$-2, which implies that the CNS-TiO$_2$/g-C$_3$N$_4$-2 heterojunction could suppress the recombination of photogenerated holes and electrons. The same result could be found in EIS spectra, as shown in Fig. 8c. The CNS-TiO$_2$/g-C$_3$N$_4$-2 has the smallest arc radius of EIS, demonstrating that the heterojunction structure of CNS-TiO$_2$ and g-C$_3$N$_4$ can effectively promote photo-induced carrier separation and charge transfer.

The main active free radicals for MO removal over the CNS-TiO$_2$/g-C$_3$N$_4$-2 heterojunction were found through free radical trapping experiments. In this study, ascorbic acid, isopropanol (IPA) and ethylenediaminetetrabutyric acid (EDTA) were employed to capture the superoxide radical ($\cdot$O$_2^-$), hydroxyl radical ($\cdot$OH) and holes (h$^+$), respectively. As shown in Fig. 9a, ascorbic acid and IPA could obviously depress the photodegradation rate of MO. Moreover, the removal efficiency of MO
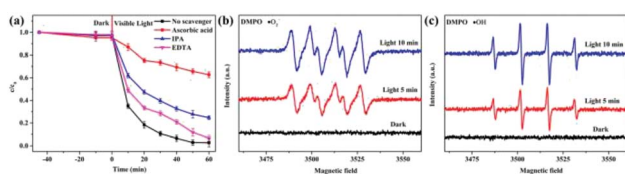
decreased significantly with the addition of ascorbic acid, indicating that $\cdot$O$_2^-$ was the main active species in MO removal. These results clearly demonstrate that $\cdot$O$_2^-$ and $\cdot$OH species play an active role in the MO photocatalytic degradation process, but the h$^+$ play a minor role.

To further confirm the above conclusions, ESR analyses were performed using 5,5-dimethyl-1-pyrroline N-oxide (DMPO) as a spin-trapping agent. In Fig. 9b, the signal of $\cdot$O$_2^-$ was not detected in the absence of light irradiation, but 1 : 1 : 1 : 1 quadruple signals[50] were observed after the sample had been irradiated by simulated solar light. In addition, the signal intensities gradually increased with the increase in illumination time. Similar phenomena were observed for $\cdot$OH (Fig. 9c). The gradually enhanced 1 : 2 : 2 : 1 characteristic signals were detected when the light was on. The results of the trapping experiments and ESR tests revealed that the $\cdot$O$_2^-$ and $\cdot$OH radicals generated in the presence of the CNS-TiO$_2$/g-C$_3$N$_4$ heterojunction photocatalysts under light irradiation were the major active components in the photocatalytic degradation process. It is noteworthy that the $\cdot$O$_2^-$ radical cannot be generated if the charge migration in the composite follows the conventional type II heterojunction mechanism. Obviously, the Z-scheme heterojunction mechanism is a better candidate to explain the enhancement mechanism of photocatalytic degradation activity of CNS-TiO$_2$/g-C$_3$N$_4$ heterojunction photocatalysts.

Based on the above experimental results and discussion, the degradation mechanism of the CNS-TiO$_2$/g-C$_3$N$_4$-2 composite catalyst for MO dye is proposed in Fig. 10. The structure of the energy band for the CNS-TiO$_2$/g-C$_3$N$_4$-2 composite catalyst is constructed based on the results of UV-vis DRS analysis and the empirical equation:[51]

$$E_{CB} = X - E^c + 0.5E_g \quad (1)$$

$$E_{VB} = E_{CB} - E_g \quad (2)$$

where E_{VB}, E_{CB}, E_g and E^c refer to the VB top potential, CB bottom potential, band gap energy and potential energy of free electrons ($\sim$4.5 eV), respectively. X is the absolute electronegativity of semiconductors, and is given by the geometric mean of

Fig. 9 (a) Influence of various scavengers on the visible-light photocatalytic activity of CNS-TiO$_2$/g-C$_3$N$_4$-2; ESR spectra of (b) DMPO $\cdot$O$_2^-$ and (c) DMPO $\cdot$OH.
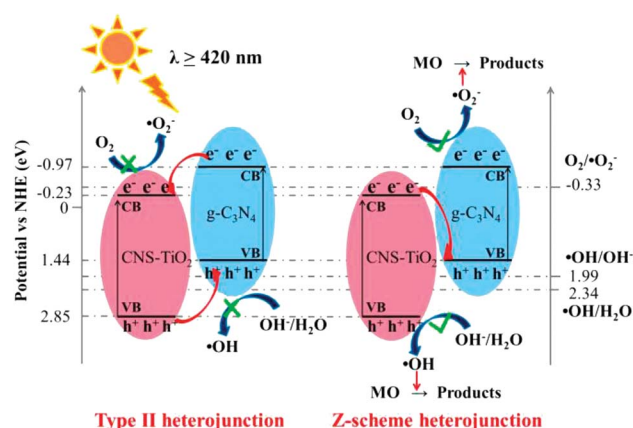

Fig. 10 Type II and Z-scheme heterojunction charge transfer mechanisms of CNS-TiO$_2$/g-C$_3$N$_4$ in the presence of MO.

first ionization energy and electronegativity of atoms evaluated from electron affinity. The X-values for g-C_3N_4 and TiO_2 are 4.73 and 5.81 eV, respectively.[52] According to the above equation, the E_{CB}-value and E_{VB}-value of CNS-TiO_2 are −0.23 and 2.85 eV, respectively, and the E_{CB}-value and E_{VB}-value of g-C_3N_4 are −0.97 and 1.44 eV, respectively.

Fig. 10 shows a possible mechanism of MO removal on CNS-TiO_2/g-C_3N_4. The photogenerated electron and hole transfer process of the g-C_3N_4 and N-TiO_2 heterojunction may show a type II or Z-scheme structure. If CNS-TiO_2/g-C_3N_4 adapts to a type II heterojunction structure, the photogenerated electrons in the CB of g-C_3N_4 transfer to the CB of CNS-TiO_2 under visible light, and the photogenerated holes in the VB of CNS-TiO_2 transfer to the VB of g-C_3N_4. However, the electrons transferred from the CB of g-C_3N_4 to the CB (−0.23 eV) of CNS-TiO_2 could not reduce O_2 into $^{\cdot}O_2^{-}$ $[E^0(O_2/^{\cdot}O_2^{-}) = -0.33$ eV $vs.$ NHE]. The holes transferred from the VB of CNS-TiO_2 to the VB (+1.44 eV) of g-C_3N_4 could not reduce H_2O/OH^{-} into $^{\cdot}OH$ $[E^0(^{\cdot}OH/OH^{-}) = $ +1.99 eV $vs.$ NHE; $E^0(H_2O/OH^{-}) = $ +2.34 eV $vs.$ NHE], which is contrary to the results of ESR and free radical capture experiments.[24] These results indicate that the type II heterojunction structure is not suitable for CNS-TiO_2/g-C_3N_4. However, CNS-TiO_2/g-C_3N_4 adapts to the Z-scheme heterojunction structure. In the Z-scheme heterojunction, the photogenerated holes in the VB of g-C_3N_4 and the photogenerated electrons in the CB of CNS-TiO_2 recombine under visible light irradiation, while the electrons and holes in the CB of g-C_3N_4 and the VB of CNS-TiO_2 are excited, respectively. MO was removed by $^{\cdot}O_2^{-}$ generated in the CB of g-C_3N_4 and $^{\cdot}OH$ generated in the VB of CNS-TiO_2. Therefore, CNS-TiO_2/g-C_3N_4 with a Z-scheme heterojunction structure can improve the separation efficiency of electrons and holes, thereby improving the photocatalytic removal efficiency of MO.

4. Conclusions

Herein, we successfully synthesized a C, N and S co-doped TiO_2/g-C_3N_4 heterojunction through a hydrothermal method followed by calcination. The formation of a Z-Scheme heterojunction in CNS-TiO_2/g-C_3N_4 could promote the photogenerated electron–hole ratio and lifetime of the composite catalyst. Meanwhile, the dopant heteroatoms expanded the photocatalytic response range to the visible light region on the basis of the heterojunction. Under the synergistic effects of the heterojunction and heteroatom doping, the photocatalytic efficiency of CNS-TiO_2/g-C_3N_4-2 for MO dye could reach 99.8% ($k = $ 0.069 min^{-1}) compared with that of the pure TiO_2 (0.1%, $k = $ 0.001 min^{-1}), and CNS-TiO_2/g-C_3N_4-2 also possesses high structural stability and catalytic activity after continuous measurements, revealing its potential as a promising material for degrading organic pollutants.

Author contributions

Huang Zhen: conceptualization, methodology, investigation, data curation, writing – original draft. Shuai Jia: supervision, review & editing. Jie Wei: review & editing. Shao Ziqiang: review & editing, project administration, funding acquisition.

Conflicts of interest

There are no conflicts to declare.

Acknowledgements

Notes and references

1 G. Mao, H. Hu, X. Liu, J. Crittenden and N. Huang, *Environ. Pollut.*, 2021, **275**, 115785.

2 V. Kumaravel, S. Mathew, J. Bartlett and S. C. Pillai, *Appl. Catal., B*, 2019, **244**, 1021–1064.

3 S. Das and H. Mahalingam, *J. Environ. Chem. Eng.*, 2019, **7**, 103289.

4 Y. Chen, W. Lu, H. Shen, Y. Gu, T. Xu, Z. Zhu, G. Wang and W. Chen, *Appl. Catal., B*, 2019, **258**, 117960.

5 A. Kumar, M. Khan, J. He and I. M. C. Lo, *Appl. Catal., B*, 2020, **270**, 118898.

6 G. Li, Y. Wu, M. Zhang, B. Chu and B. Li, *Ind. Eng. Chem. Res.*, 2019, **58**, 1.

7 Y. Yu, W. Xu, J. Fang, D. Chen, T. Pan, W. Feng, Y. Liang and Z. Fang, *Appl. Catal., B*, 2020, **268**, 118751.

8 J. Z. A. B. Huang and A. Mao Wu, *Appl. Catal., B*, 2019, **241**, 159–166.

9 H. Yi, D. Huang, L. Qin, G. Zeng, C. Lai, M. Cheng, S. Ye, B. Song, X. Ren and X. Guo, *Appl. Catal., B*, 2018, **239**, 408–424.

10 Z. Wei, F. Liang, Y. Liu, W. Luo, J. Wang, W. Yao and Y. Zhu, *Appl. Catal., B*, 2017, **201**, 600–606.

11 L. Yang, X. Bai, J. Shi, X. Du, L. Xu and P. Jin, *Appl. Catal., B*, 2019, **256**, 117759.

12 W. Wang, J. Fang, S. Shao, M. Lai and C. Lu, *Appl. Catal., B*, 2017, **217**, 57–64.

13 X. An, C. Hu, H. Liu and J. Qu, *J. Mater. Chem. A*, 2017, **5**, 24989–24994.

14 W. Zhou, Z. Yin, Y. Du, X. Huang, Z. Zeng, Z. Fan, H. Liu, J. Wang and H. Zhang, *Small*, 2013, **9**, 140–147.

15 X. Du, X. Bai, L. Xu, L. Yang and P. Jin, *Chem. Eng. J.*, 2020, **384**, 123245.

16 J. Huang, D. Li, R. Li, Q. Zhang, T. Chen, H. Liu, Y. Liu, W. Lv and G. Liu, *Chem. Eng. J.*, 2019, **374**, 242–253.

17 H. Deng, X. Wang, L. Wang, Z. Li, P. Liang, J. Ou, K. Liu, L. Yuan, Z. Jiang, L. Zheng, Z. Chai and W. Shi, *Chem. Eng. J.*, 2020, **401**, 125977.

18 J. Ni, W. Wang, D. Liu, Q. Zhu, J. Jia, J. Tian, Z. Li, X. Wang and Z. Xing, *J. Hazard. Mater.*, 2020, 124432.

19 B. Bajorowicz, M. P. Kobylański, A. Gołąbiewska, J. Nadolna, A. Zaleska-Medynska and A. Malankowska, *Adv. Colloid Interface Sci.*, 2018, **256**, 352–372.

20 H. Tang, Q. Shang, Y. Tang, X. Yi, Y. Wei, K. Yin, M. Liu and C. Liu, *J. Hazard. Mater.*, 2020, **384**, 121248.

21 J. Huang, D. Li, R. Li, P. Chen, Q. Zhang, H. Liu, W. Lv, G. Liu and Y. Feng, *J. Hazard. Mater.*, 2020, **386**, 121634.

22 G. Sui, J. Li, L. Du, Y. Zhuang, Y. Zhang, Y. Zou and B. Li, *J. Alloys Compd.*, 2020, **823**, 153851.

23 Z. Hu, X. Cai, Z. Wang, S. Li, Z. Wang and X. Xie, *J. Hazard. Mater.*, 2019, **380**, 120812.

24 Y. Wang, L. Rao, P. Wang, Z. Shi and L. Zhang, *Appl. Catal., B*, 2020, **262**, 118308.

25 G. Fang, M. Li, H. Shen, S. Yang and J. Israr, *Mater. Sci. Semicond. Process.*, 2021, **121**, 105374.

26 S. Liu and W. Lin, *J. Hazard. Mater.*, 2019, **368**, 468–476.

27 X. Li, S. Yang, J. Sun, P. He, X. Xu and G. Ding, *Carbon*, 2014, **78**, 38–48.

28 L. Ma, H. Fan, K. Fu, S. Lei, Q. Hu, H. Huang and G. He, *ACS Sustainable Chem. Eng.*, 2017, **5**, 7093–7103.

29 W. Wang, W. Zhu, L. Mao, J. Zhang, Z. Zhou and G. Zhao, *J. Colloid Interface Sci.*, 2019, **557**, 227–235.

30 K. Hu, R. Li, C. Ye, A. Wang, W. Wei, D. Hu, R. Qiu and K. Yan, *J. Cleaner Prod.*, 2020, **253**, 120055.

31 H. Xu, J. Yan, X. She, L. Xu, J. Xia, Y. Xu, Y. Song, L. Huang and H. Li, *Nanoscale*, 2014, **6**, 1406–1415.

32 L. Ma, G. Wang, C. Jiang, H. Bao and Q. Xu, *Appl. Surf. Sci.*, 2018, **430**, 263–272.

33 R. Hao, G. Wang, C. Jiang, H. Tang and Q. Xu, *Appl. Surf. Sci.*, 2017, **411**, 400–410.

34 W. Zhang, X. Xiao, Y. Li, X. Zeng, L. Zheng and C. Wan, *Appl. Surf. Sci.*, 2016, **389**, 496–506.

35 F. Wu, X. Li, W. Liu and S. Zhang, *Appl. Surf. Sci.*, 2017, **405**, 60–70.

36 X. Wei, H. Wang, X. Wang and W. Jiang, *Appl. Surf. Sci.*, 2017, **426**, 1271–1280.

37 X. Liu, W. Li, R. Hu, Y. Wei, W. Yun, P. Nian, J. Feng and A. Zhang, *Chemosphere*, 2020, **249**, 126093.

38 J. Wang, G. Wang, B. Cheng, J. Yu and J. Fan, *Chin. J. Catal.*, 2021, **42**, 56–68.

39 M. Jiménez-Salcedo, M. Monge and M. T. Tena, *Chemosphere*, 2019, **215**, 605–618.

40 A. Sudhaik, P. Raizada, P. Shandilya, D. Jeong, J. Lim and P. Singh, *J. Ind. Eng. Chem.*, 2018, **67**, 28–51.

41 R. S. Sutar, R. P. Barkul, S. D. Delekar and M. K. Patil, *Arabian J. Chem.*, 2020, 4.

42 A. Mishra, A. Mehta, S. Kainth and S. Basu, *J. Alloys Compd.*, 2018, **764**, 406–415.

43 Z. Meng, B. Zhou, J. Xu, Y. Li and H. Tian, *Chem. Res. Chin. Univ.*, 2020, 4.

44 B. Yu, F. Meng, M. W. Khan, R. Qin and X. Liu, *Ceram. Int.*, 2020, 5.

45 Y. Wang, Y. He, Q. Lai and M. Fan, *J. Environ. Sci.*, 2014, **26**, 2139–2177.

46 S. Narzary, K. Alamelu, V. Raja and B. M. Jaffar Ali, *J. Environ. Chem. Eng.*, 2020, **8**, 104373.

47 M. R. Al-Mamun, S. Kader, M. S. Islam and M. Z. H. Khan, *J. Environ. Chem. Eng.*, 2019, 7, 103248.

48 K. Wang, J. Li and G. Zhang, *ACS Appl. Mater. Interfaces*, 2019, **11**, 27686–27696.

49 X. Zheng, Y. Liu, X. Liu, Q. Li and Y. Zheng, *Ecotoxicol. Environ. Saf.*, 2021, **210**, 111866.

50 Y. Diao, M. Yan, X. Li, C. Zhou, B. Peng, H. Chen and H. Zhang, *Colloids Surf., A*, 2020, **594**, 124511.

51 Y. Li, M. Gu, X. Zhang, J. Fan, K. Lv, S. A. C. Carabineiro and F. Dong, *Mater. Today*, 2020, **41**, 270–303.

52 H. Yang, C. Yang, N. Zhang, K. Mo, Q. Li, K. Lv, J. Fan and L. Wen, *Appl. Catal., B*, 2021, **285**, 119801.